RSC Advances

ROYAL SOCIETY OF CHEMISTRY

www.rsc.org/advances

Journal Name

ARTICLE TYPE

A freestanding composite film electrode stacked from hierarchical electrospun SnO$_2$ nanorods and graphene sheets for reversible lithium storage

Simin Jiang,[a] Bote Zhao,[a] Ran Ran,*[a] Rui Cai,[a] Moses O. Tadé[c] and Zongping Shao*[a,b,c]

A freestanding hierarchical SnO$_2$ nanorod/graphene composite film electrode was designed and fabricated by a general route including electrospinning and film casting processes. With dual adaptable strategies (hierarchical nanorod structure and graphene "overcoats"), the composite film electrode exhibited enhanced cycling stability.

Since Sony Corporation developed and released the first commercial lithium-ion battery (LIB) in 1991, rechargeable LIBs have become one of the most popular power sources for portable personal electronics due to their high energy density, environmental compatibility and the fact that they display no memory effect.[1-3] However, the rapid development of personal electronic devices has led to a rapid growth in the demand for higher capacity LIBs. Tin oxide (SnO$_2$) is a promising candidate as an anode for LIBs due to its extremely high theoretical capacity (782 mA h g^{-1}), which is more than twice that of commercial graphite anodes (372 mA h g^{-1}).[4,5] The drawback to conventional bulk SnO$_2$-based materials is their characteristically large variation in volume (>200%) during the lithium insertion/extraction process,[6,7] which easily leads to pulverization and delamination of the electrode from the current collector; thus, a quick decay of the electrochemical performance is often observed. To solve these problems, two leading approaches have been applied. One method is the preparation of various SnO$_2$ nanostructures, such as nanoparticles,[8] nanotubes,[9] nanoboxes,[10] nanowires,[11,12] nanorod arrays[13] and hollow spheres.[14,15] Another effective method is the synthesis of SnO$_2$-based composites, such as SnO$_2$/Cu,[16] SnO$_2$@carbon,[17-19] SnO$_2$/graphene[20,21] and SnO$_2$/carbon nanotubes.[22,23]. SnO$_2$ nanostructures are able to release mechanical strain, and the introduction of the void space from the special structures and carbon are helpful in accommodating the volume variation during the lithium insertion/extraction process.

Recently, there has been a growing interest in the development of flexible, lightweight and high-power thin-film electrodes for LIBs.[24-26] During the conventional electrode preparation process, a conductive agent and binder are necessary.[10,21,27,28] The binder, which is insulating and electrochemically inactive, will decrease the effect of the current collection and reduce the contact area between the active material and the liquid electrolyte. By applying thin films as binder-free anodes for LIBs, the conventional process of electrode preparation, which involves slurry mixing and coating, is replaced, and the additional conductive agent and binder are avoided. This results in a reduction in the electrode resistance and an improvement of the volumetric/gravimetric energy densities.

Electrospinning is recognized as a simple and versatile method for fabricating nanofibers from various raw materials.[26,29-31] Meanwhile, a nonwoven thin film can be easily obtained by the deposition of nanofibers using the electrospinning technique. In contrast to other methods for producing thin films, there is no requirement of complex equipment or special substrates for electrospinning. Moreover, electrospinning is a continuous process with a high production rate, and the produced film is freestanding. SnO$_x$-based fibers have been successfully fabricated using electrospinning combined with a calcination process.[6,32-35] However, most of these fibers were converted into electrodes using the conventional electrode preparation because SnO$_x$ itself is inflexible and the film after calcination in air has poor mechanical strength. Introduction of carbon into the electrospun film could enhance the mechanical properties and make the film flexible.[26,35] However, a high temperature was necessary for carbonization of the polymer; SnO$_2$ is easily reduced to Sn in the presence of carbon and reducing gas (*e.g.,* CO), which is produced from the polymer decomposition at a high temperature. The melting point of Sn is only 232 °C,[36] which leads to rapid growth of Sn/SnO$_x$ particles. Thus, complicated fabrication steps, such as coaxial electrospinning [32] or the use of high carbon contents (>70 wt%) [35], were needed to prevent agglomeration of the SnO$_x$ nanoparticles. Thus, it is difficult to fabricate flexible freestanding electrospun films with a high content of SnO$_x$ through a facile electrospinning method. Recently, graphene oxide (GO) was found to be easily assembled into films due to the attached oxygen-containing functional groups.[37,38] After a deoxygenating process, a freestanding conductive graphene film could be obtained. However, the ordinary pure graphene film exhibited poor electrochemical performance due to the loss of its large surface area caused by the tight stacking of the graphene sheets.[39] Thus, the preparation of composite

Fig. 1. Schematic illustration of the preparation of the hierarchical SnO$_2$ nanorod/graphene film.

Fig. 2. (a, b) FE-SEM images and (c) TEM image of the SnO$_2$ nanorods after the sedimentation separation process; (d) the SAED pattern of the SnO$_2$ nanorods; (b) is a magnified image.

films may be a promising strategy. The interconnecting graphene matrix may show superior electrical conductivity, and the high flexibility of the graphene sheets could be able to accommodate the large volume variation of the active material during the lithium insertion/extraction process.

In this work, a freestanding hierarchical SnO$_2$ nanorod/graphene composite film was prepared as a binder-free anode for LIBs. The hierarchical SnO$_2$ nanorods, which are composed of SnO$_2$ nanoparticles 11–20 nm in diameter, were fabricated by facile electrospinning and sedimentation separation processes. The hierarchical nanorod structure is an adaptable design for accommodating the large volume variation during the charge/discharge cycles. The compact conductive graphene sheets in the formed composite film act as the other adaptable strategy. With these dual adaptable strategies, the hierarchical SnO$_2$ nanorod/graphene composite film electrode exhibited a high reversible capacity and enhanced cycling stability.

Fig. 1 shows the preparation process of hierarchical SnO$_2$ nanorods/graphene film. SnO$_2$ nanofibers were first fabricated using an electrospinning method with a subsequent calcination process (500 $^{\circ}$C in air). Then a facile sedimentation separation process was used for obtaining well-dispersed SnO$_2$ nanorods from the SnO$_2$ nanofibers. And a subsequent film casting process together with GO solution was conducted for the formation of composite film. Finally, a calcining treatment in Ar was carried out to obtain the SnO$_2$ nanorods/graphene film. The morphology and microstructure of the electrospun SnO$_2$ nanofibers after calcination were investigated by field-emission scanning electron microscopy (FE-SEM). Typical FE-SEM images are shown in **Fig. S1** (see ESI†). The diameters of the nanofibers were mostly 210±90 nm (**Fig. S1a**). There was also a small amount of ultrafine nanofibers with diameters of ~70 nm, which may have formed due to the fluctuations during the electrospinning process. A magnified image (**Fig. S1b**) reveals that the surface of these SnO$_2$ nanofibers was rough. Each nanofiber was in a hierarchical structure composed of ultrafine SnO$_2$ nanoparticles.

For the film preparation, the direct dispersion of the as-obtained SnO$_2$ nanofibers in the GO solution was first attempted using a probe ultrasonic homogenizer. The solution was then transferred to the polytetrafluoroethylene (PTFE) cell and placed in the drying oven at 60 °C. However, before all of the solvent (water) could evaporate, parts of the white nanofibers sunk to the bottom. After drying, one side of the obtained film was white in color, suggesting that large
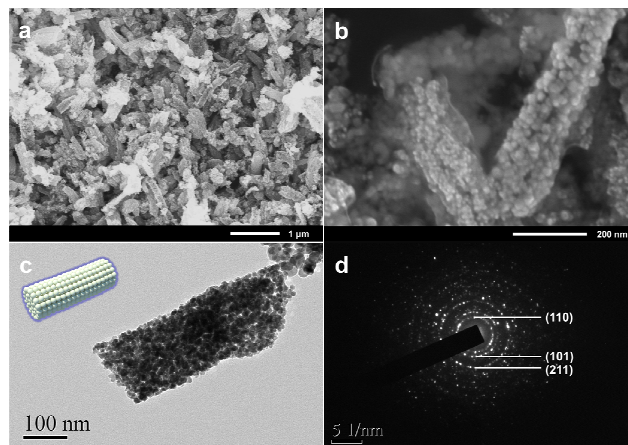
amounts of SnO$_2$ nanofibers were not sandwiched between the graphene sheets. Thus, a facile sedimentation separation process was designed to obtain well-dispersed SnO$_2$ nanorods. Briefly, the SnO$_2$ nanofibers were shortened and dispersed in the deionized water by a probe-ultrasonically treating. (Details see ESI†) The as-obtained SnO$_2$ nanorods-contained solution was standing for about 24 h at room temperature. The upper solution with suspended SnO$_2$ nanorods was transferred and dried to obtain the well-dispersed SnO$_2$ nanorods.

As shown in **Fig. 2a**, after the sedimentation separation process, the length of the SnO$_2$ nanorods was shortened to a few hundred nanometers from the initial length of >10 μm for the electrospun SnO$_2$ nanofibers. In addition, the SnO$_2$ nanorods with smaller diameters were successfully separated out. The diameter of the SnO$_2$ nanorods was only ~140 nm, in comparison with the initial electrospun SnO$_2$ nanofibers, suggesting that the facile sedimentation separation process combined with the probe ultrasonic treatment successfully converted the long electrospun SnO$_2$ nanofibers into well-dispersed SnO$_2$ nanorods that would not sink to the bottom during the film casting process. **Fig. 2b** shows two individual SnO$_2$ nanorods with diameters of approximately 140 nm. The hierarchical structure was maintained after the sedimentation separation process. The crystallographic structure of the SnO$_2$ nanorods was examined using X-ray diffraction (XRD), and the results are shown in **Fig. S2** (see ESI†). The pattern could be indexed as tetragonal SnO$_2$ (JCPDS, No.: 41-1445). The average crystalline grain size of the SnO$_2$ nanorods was estimated to be approximately 14 nm from the (110) peak, according to the Scherrer equation. The morphology and phase structure of the SnO$_2$ nanorods were further examined using transmission electron microscopy (TEM) and selective area electron diffraction (SAED). As shown in **Fig. 2c**, the hierarchical structure of the SnO$_2$ nanorod was clearly demonstrated, indicating that the nanorod was stacked from ultrafine primary SnO$_2$ nanoparticles with diameters of 11–20 nm. The specific surface area of the SnO$_2$ nanorods was determined to be 42.7 m^2 g^{-1} using the Brunauer-Emmett-Teller (BET) method. The porous hierarchical structure was mainly caused by the gases produced from the decomposition of the organic material in the precursor. During the

calcination process in air, the organic material was oxidized to gas, while the (IV) source was converted to solid crystallized SnO_2. The produced gases diffused rapidly at the high temperature, which prevented the agglomeration of the SnO_2
5 particles. Due to the relatively low calcination temperature (500 °C), the hierarchical structure stacked with SnO_2 nanoparticles was retained, thus fulfilling the first adaptable strategy. **Fig. 2d** shows the SAED pattern of the SnO_2 nanorods, which is composed of a series of concentric rings
10 corresponding to the (110), (101) and (211) lattice planes, suggesting the polycrystalline character of the nanorods and the tetragonal SnO_2 phase structure.
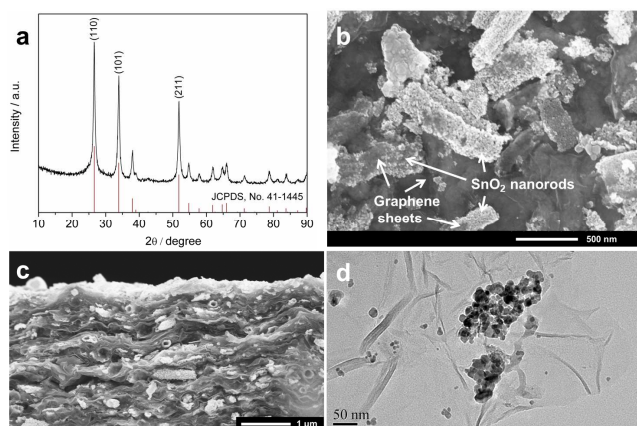

Fig. 3. (a) XRD pattern, (b, c) FE-SEM images ((b) surface and (c) cross-
15   section) and (d) TEM image of the SnO_2 nanorod/graphene film.

   By using the well-dispersed SnO_2 nanorods together with the GO solution for film casting, a homogeneous SnO_2 nanorod/graphene composite film was easily fabricated. The phase structure and purity of the SnO_2 nanorod/graphene
20 composite film were investigated by XRD. As shown in **Fig. 3a**, the composite after the calcination in Ar at 500 °C for 3 h also exhibited a tetragonal SnO_2 phase structure (JCPDS, No.: 41-1445), free from Sn or SnO impurity phases. The broadened peak of graphene was merged with the (110) peak
25 of SnO_2. The intensity and width of the peaks were similar in comparison with the pattern of the pure SnO_2 nanorods, suggesting that the additional calcination did not significantly affect the SnO_2 crystalline size. **Fig. 3b** presents the surface morphology of the SnO_2 nanorod/graphene composite film.
30 The hierarchical structure of the SnO_2 nanorods was well maintained. There were some SnO_2 nanorods deposited on the surface of the graphene sheets, and the graphene sheets covered the SnO_2 nanorods. It should be mentioned that the surface morphology of both sides of the composite film was
35 similar, indicating a high homogeneity of the composite film. **Fig. 3c** shows the cross-sectional morphological image of the SnO_2 nanorod/graphene composite film. It is clear that the nanorods (some of them are hollow) were well sandwiched between the graphene sheets. During the film casting process,
40 the SnO_2 nanorods and GO sheets were randomly deposited and assembled into a composite film with the evaporation of water. After calcination, the conductive graphene sheets in the composite film acted as "overcoats" of the SnO_2 nanorods to provide the second adaptable strategy. Graphene structure was

45 confirmed by the TEM observation (**Fig. 3d**) and the XPS analysis (**Fig. S3**, see ESI†). The Raman spectrum (**Fig. S4**, see ESI†) shows two broad peaks at approximately 1352 and 1598 cm^{-1}, corresponding to the D (defect-related) and G (doubly degenerate zone center E_{2g} mode) bands of the carbon
50 material. The strong D band suggests the presence of a large numbers of defects for the graphene in the composite film. The carbon content in the composite was 44.6 wt.%, estimated from the thermogravimetric analysis (TGA) in air (**Fig. S5**, see ESI†).
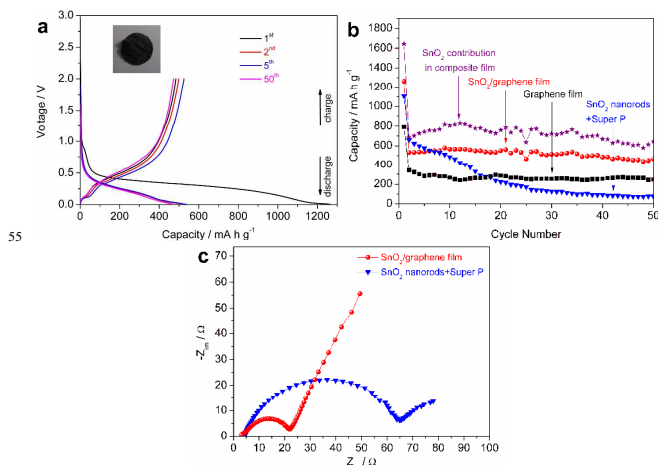

Fig. 4. (a) The discharge/charge curves of SnO_2 nanorod/graphene film at
   100 mA g^{-1} between 0.005 and 2.0 V, the inset is a digital photo; (b) the
   cycling performance (discharge capacity) of the various electrodes at 100
60   mA g^{-1} between 0.005 and 2.0 V: i) SnO_2 nanorod/graphene film, ii)
   graphene film and iii) SnO_2 nanorod electrode prepared using a slurry
   coating technique with Super P; (c) electrochemical impedance spectra of
   the cells with SnO_2 nanorod/graphene film and graphene-free SnO_2
   nanorod+Super P electrode.

65   The electrochemical performance of the hierarchical SnO_2 nanorod/graphene composite film (inset of **Fig. 4a**) was evaluated as the anode in a half cell without any additional conductive agent or binder. **Fig. 4a** shows representative discharge/charge curves of the SnO_2 nanorod/graphene
70 composite film electrode. The first discharge capacity of the composite film was 1264 mA h g^{-1} (calculated based on the mass of SnO_2 nanorods and grahpene), and the subsequent charge capacity was 484 mA h g^{-1}. The oulombic efficiency for the first cycle was only 38%. The low coulombic
75 efficiency was due to the irreversible formation of lithium oxide (Li^+ undergoes a conversion reaction with SnO_2) and the solid-electrolyte interface (SEI) layer.[6,10] However, the Coulombic efficiency increased to 94% at the second cycle and almost kept higher than 95% at subsequent cycles (**Fig.**
80 **S6**). And the cycling performance after the first cycle was relatively stable through 50 cycles (**Fig. 4a&b**). A pure graphene film electrode was also prepared in a similar fashion and investigated as free-standing electrode, delivering discharge capacities of 792, 341, 281 and 247 mA h g^{-1} at the
85 first, second, fifth and 50th cycles, respectively. These values were substantially lower than those of the hierarchical SnO_2 nanorod/graphene composite film. For comparison, the SnO_2 nanorods were also prepared to be a graphene-free electrode using a conventional slurry coating procedure. As shown in

Fig. 4b, The discharge capacity was 1103 mA h g^{-1} (calculated based on the mass of SnO$_2$ nanorods and Super P) at first cycle, and decreased gradually to 660 mA h g^{-1} at the second cycle, 574 mA h g^{-1} at the fifth cycle and to only 75 mA h g^{-1} at the 50th cycle. Conversely, the SnO$_2$ nanorod/graphene composite film electrode exhibited stable cycling performance with a capacity of 467 mA h g^{-1} after 50 cycles, as shown in **Fig. 4a&b**. **Fig. 4c** shows electrochemical impedance spectra of the cells with different electrodes. The resistance of SnO$_2$ nanorod/graphene film was lower than that of graphene-free SnO$_2$ nanorod electrode, which could be attributed to the presence of interconnecting graphene matrix in the composite film. The capacity contribution of the SnO$_2$ nanorods in the composite film was also calculated on the basis of the capacities of the composite film and graphene film with a carbon content of 44.6 wt.%, $C_{SnO2}=(C_{composite} - C_{graphene\ film} \times 0.446)/0.554$. The results are also shown in **Fig. 4b**, indicating a stable SnO$_2$ capacity contribution of around 720 mA h g^{-1} (close to the theoretical capacity of 782 mA h g^{-1}) through 50 cycles. The improved cycling stability can be attributed to the unique features of the hierarchical SnO$_2$ nanorod/graphene film. The hierarchical nanorod structure composed of SnO$_2$ nanoparticles performed as the first adaptable strategy, in which the ultrafine nanoparticles could release mechanical strain, and the void space created by the particle stacking offered a buffer zone to accommodate the volume variation during the lithium insertion/extraction process. Moreover, the nanorod structure with a small diameter of ~140 nm also benefited the lithium ion transport. The stacked graphene sheets in the composite film acted as overcoats for the other adaptable strategy. Because the graphene sheets are flexible and interconnected, they were able to accommodate the large volume variation of the SnO$_2$ nanorods. The interconnected graphene sheets also acted as a three-dimensional conductive network for electron transport. In addition, the composite film was applied directly as the working electrode, eliminating the use of an insulating and electrochemically inactive binder.

In summary, we have successfully prepared a freestanding hierarchical SnO$_2$ nanorod/graphene composite film using an electrospinning and film casting route. The well-dispersed SnO$_2$ nanorods could be easily obtained from electrospun SnO$_2$ nanofibers by a facile sedimentation separation process. By applying the composite film with dual adaptable strategies (hierarchical SnO$_2$ nanorod structure and graphene overcoats) as a binder-free anode for LIBs, it exhibited an enhanced cycling performance with a capacity of 467 mA h g^{-1}, even after 50 charge-discharge cycles. We believe that the facile sedimentation separation process could also be used to separate various nano-materials and that the general synthesis route presented here could also be used to fabricate other composite anodes or cathodes for reversible lithium storage.

Acknowledgements

Notes and references

^{a} State Key Laboratory of Materials-Oriented Chemical Engineering, College of Chemistry & Chemical Engineering, Nanjing University of Technology, No.5 Xin Mofan Road, Nanjing, 210009, PR China; Fax: +86 25 83172242; Tel: +86 25 83172256; E-mail: ranr@njut.edu.cn, shaozp@njut.edu.cn.
^{b} College of Energy, Nanjing University of Technology, No.5 Xin Mofan Road, Nanjing, 210009, PR China
^{c} Department of Chemical Engineering, Curtin University, WA 6845, Australia

† Electronic Supplementary Information (ESI) available: Experimental details, FE-SEM, XRD, Raman, TGA. See DOI: 10.1039/b000000x/

1 J. M. Tarascon and M. Armand, *Nature*, 2001, **414**, 359.
2 M. Armand and J. M. Tarascon, *Nature*, 2008, **451**, 652.
3 B. T. Zhao, X. Yu, R. Cai, R. Ran, H. T. Wang and Z. P. Shao, *J. Mater. Chem.*, 2012, **22**, 2900.
4 S. M. Paek, E. Yoo and I. Honma, *Nano Lett.*, 2009, **9**, 72.
5 B. Zhang, Q. B. Zheng, Z. D. Huang, S. W. Oh and J. K. Kim, *Carbon*, 2011, **49**, 4524.
6 L. M. Li, X. M. Yin, S. Liu, Y. G. Wang, L. B. Chen and T. H. Wang, *Electrochem. Commun.*, 2010, **12**, 1383.
7 X. Wang, X. Cao, L. Bourgeois, H. Guan, S. Chen, Y. Zhong, D.-M. Tang, H. Li, T. Zhai, L. Li, Y. Bando and D. Golberg, *Adv. Funct. Mater.*, 2012, **22**, 2682.
8 H. J. Ahn, H. C. Choi, K. W. Park, S. B. Kim and Y. E. Sung, *J. Phys. Chem. B*, 2004, **108**, 9815.
9 J. F. Ye, H. J. Zhang, R. Yang, X. G. Li and L. M. Qi, *Small*, 2010, **6**, 296.
10 Z. Y. Wang, D. Y. Luan, F. Y. C. Boey and X. W. Lou, *J. Am. Chem. Soc.*, 2011, **133**, 4738.
11 M. S. Park, G. X. Wang, Y. M. Kang, D. Wexler, S. X. Dou and H. K. Liu, *Angew. Chem. Int. Ed.*, 2007, **46**, 750.
12 H. Kim and J. Cho, *J. Mater. Chem.*, 2008, **18**, 771.
13 J. P. Liu, Y. Y. Li, X. T. Huang, R. M. Ding, Y. Y. Hu, J. Jiang and L. Liao, *J. Mater. Chem.*, 2009, **19**, 1859.
14 X. W. Lou, Y. Wang, C. L. Yuan, J. Y. Lee and L. A. Archer, *Adv. Mater.*, 2006, **18**, 2325.
15 J. S. Chen, C. M. Li, W. W. Zhou, Q. Y. Yan, L. A. Archer and X. W. Lou, *Nanoscale*, 2009, **1**, 280.
16 W. Xu, N. L. Canfield, D. Y. Wang, J. Xiao, Z. M. Nie and J. G. Zhang, *J. Power Sources*, 2010, **195**, 7403.
17 Y. Wang, H. C. Zeng and J. Y. Lee, *Adv. Mater.*, 2006, **18**, 645.
18 B. H. Zhang, X. Y. Yu, C. Y. Ge, X. M. Dong, Y. P. Fang, Z. S. Li and H. Q. Wang, *Chem. Commun.*, 2010, **46**, 9188.
19 P. Wu, N. Du, H. Zhang, J. X. Yu, Y. Qi and D. R. Yang, *Nanoscale*, 2011, **3**, 746.
20 C. H. Xu, J. Sun and L. Gao, *Nanoscale*, 2012, **4**, 5425.
21 S. K. Park, S. H. Yu, N. Pinna, S. Woo, B. Jang, Y. H. Chung, Y. H. Cho, Y. E. Sung and Y. Piao, *J. Mater. Chem.*, 2012, **22**, 2520.
22 Z. H. Wen, Q. Wang, Q. Zhang and J. H. Li, *Adv. Funct. Mater.*, 2007, **17**, 2772.
23 Y. H. Jin, K. M. Min, S. D. Seo, H. W. Shim and D. W. Kim, *J. Phys. Chem. C*, 2011, **115**, 22062.
24 V. L. Pushpparaj, M. M. Shaijumon, A. Kumar, S. Murugesan, L. Ci, R. Vajtai, R. J. Linhardt, O. Nalamasu and P. M. Ajayan, *Proc. Natl. Acad. Sci. U. S. A.*, 2007, **104**, 13574.
25 N. Li, Z. P. Chen, W. C. Ren, F. Li and H. M. Cheng, *Proc. Natl. Acad. Sci. U. S. A.*, 2012, **109**, 17360.
26 B. T. Zhao, R. Cai, S. M. Jiang, Y. J. Sha and Z. P. Shao, *Electrochim. Acta*, 2012, **85**, 636.
27 Y. K. Zhou, J. Wang, Y. Y. Hu, R. O'Hayre and Z. P. Shao, *Chem. Commun.*, 2010, **46**, 7151.
28 T. Yuan, R. Cai, K. Wang, R. Ran, S. M. Liu and Z. P. Shao, *Ceram. Int.*, 2009, **35**, 1757.

29 D. Li and Y. N. Xia, *Adv. Mater.*, 2004, **16**, 1151.
30 Z. X. Dong, S. J. Kennedy and Y. Q. Wu, *J. Power Sources*, 2011, **196**, 4886. 改 JMCA
31 T. Yuan, B. T. Zhao, R. Cai, Y. K. Zhou and Z. P. Shao, *J. Mater. Chem.*, 2011, **21**, 15041.
32 Y. Yu, L. Gu, C. L. Wang, A. Dhanabalan, P. A. van Aken and J. Maier, *Angew. Chem. Int. Ed.*, 2009, **48**, 6485.
33 Y. Yu, L. Gu, C. B. Zhu, P. A. van Aken and J. Maier, *J. Am. Chem. Soc.*, 2009, **131**, 15984.
34 C. A. Bonino, L. W. Ji, Z. Lin, O. Toprakci, X. W. Zhang and S. A. Khan, *ACS Appl. Mater. Interfaces*, 2011, **3**, 2534.
35 B. Zhang, Y. Yu, Z. D. Huang, Y. B. He, D. Jang, W. S. Yoon, Y. W. Mai, F. Y. Kang and J. K. Kim, *Energy Environ. Sci.*, 2012, **5**, 9895.
36 D. Deng and J. Y. Lee, *Angew. Chem. Int. Ed.*, 2009, **48**, 1660.
37 Z. Niu, J. Chen, H. H. Hng, J. Ma and X. Chen, *Adv. Mater.*, 2012, **24**, 4144.
38 S. Pei, J. Zhao, J. Du, W. Ren and H.-M. Cheng, *Carbon*, 2010, **48**, 4466.
39 C. Y. Wang, D. Li, C. O. Too and G. G. Wallace, *Chem. Mater.*, 2009, **21**, 2604.